Supporting Information

$Cs_3Bi_2I_9$ Nanodiscs with Phase and Bi (III) State Stability under Reductive Potential or Illumination for H_2 Generation from Diluted Aqueous HI

Sonu Pratap Chaudhary,[1] Subhajit Bhattacharjee,[1] Vishwadeepa Hazra,[1] Sanjib Shyamal,[2] Narayan Pradhan,[2] and Sayan Bhattacharyya[1,*]

[1]*Department of Chemical Sciences and Centre for Advanced Functional Materials, Indian Institute of Science Education and Research (IISER) Kolkata, Mohanpur - 741246, India*
[2]*School of Materials Sciences, Indian Association for the Cultivation of Science, Kolkata700032, India*

**Email for correspondence: sayanb@iiserkol.ac.in*

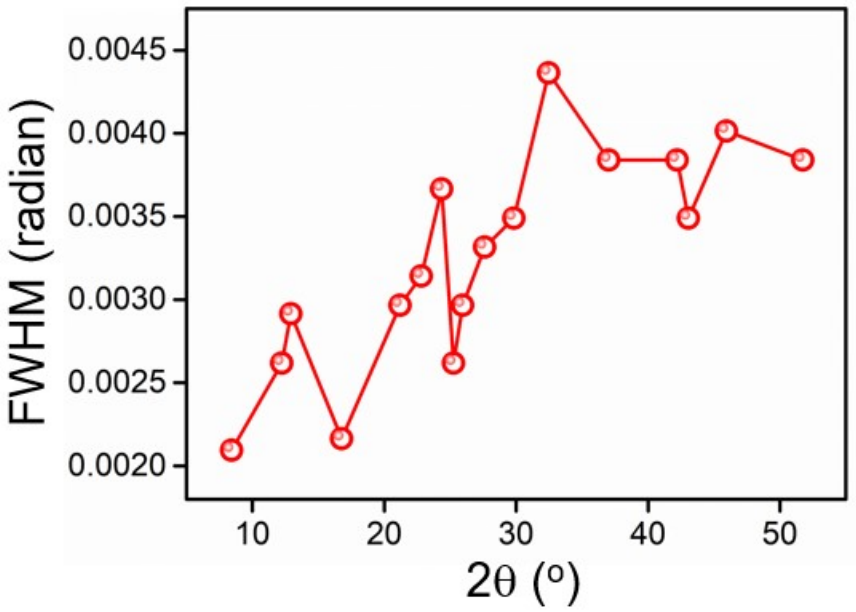

Figure S1. Variation of FWHM with 2θ for $Cs_3Bi_2I_9$ NDs.

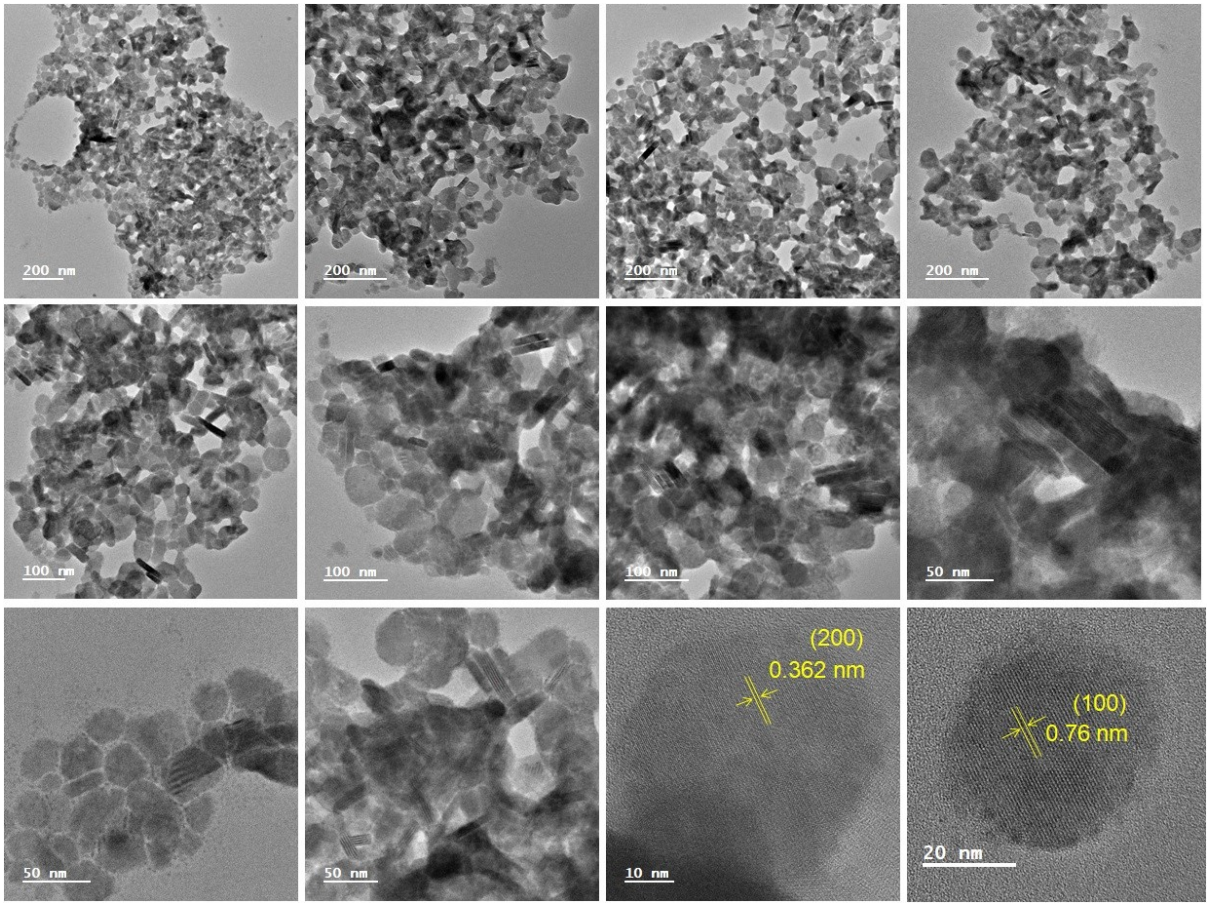

Figure S2. Additional TEM and HRTEM images of $Cs_3Bi_2I_9$ NDs.

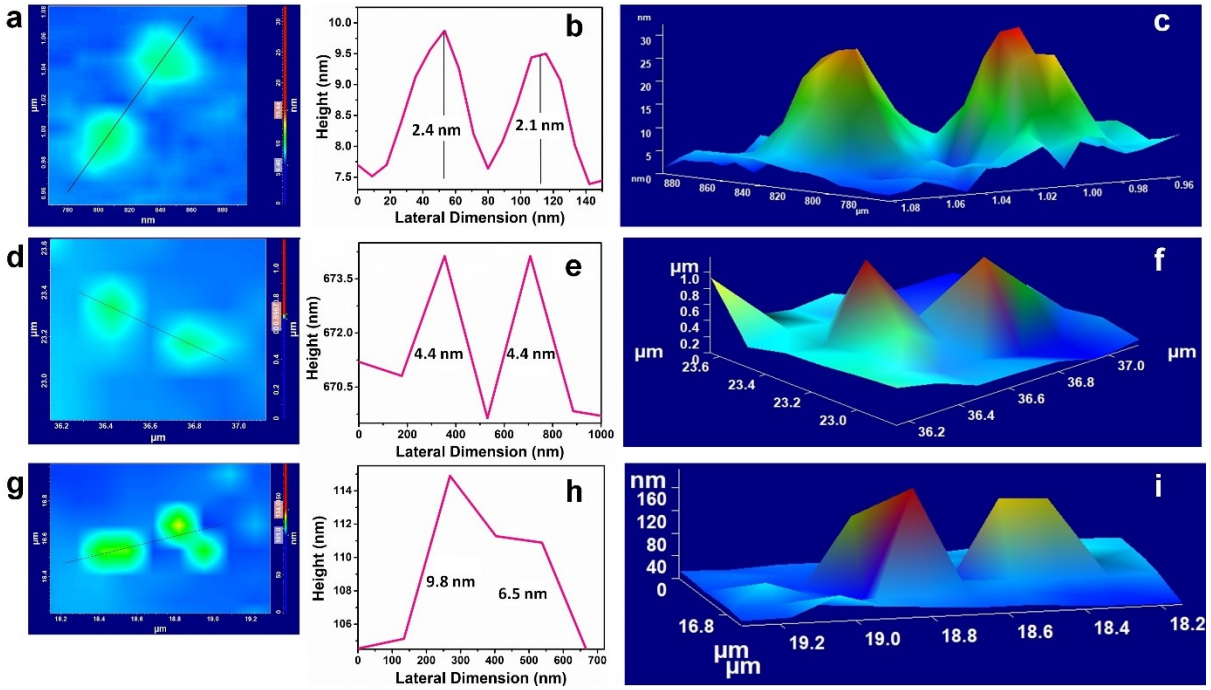

Figure S3. AFM image, height profile and 3D AFM image of $Cs_3Bi_2I_9$ NDs prepared with reaction times of (a-c) 3 s, (d-f) 15 s, and (g-i) 60 s.

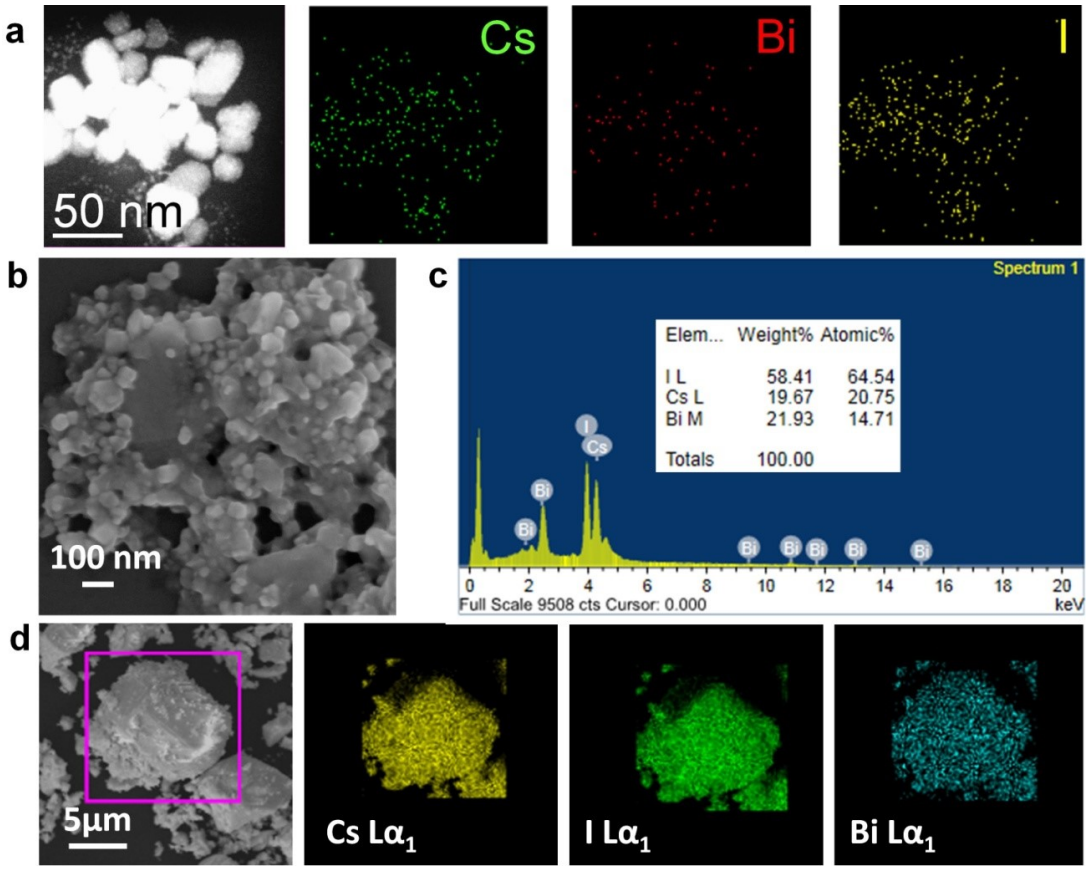

Figure S4. (a) HAADF-STEM mapping showing the elemental distribution. (b) FE-SEM image of agglomerated $Cs_3Bi_2I_9$ ND clusters. (c) EDAX spectrum showing surface elemental stoichiometry of the NDs. (d) Elemental mapping from a selected region shown on the left.

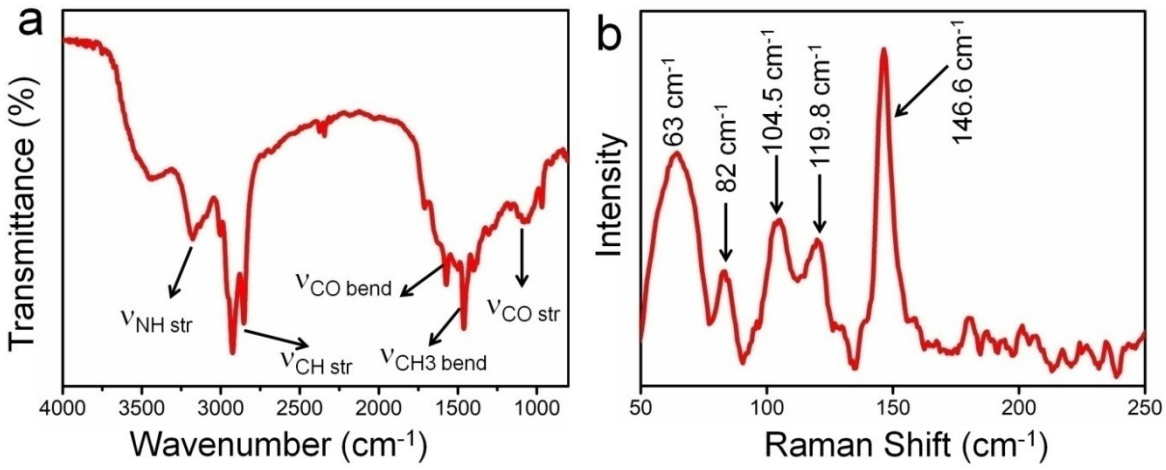

Figure S5. (a) FTIR and (b) Raman spectra of $Cs_3Bi_2I_9$ NDs.

Raman spectral bands	Assignment
63 cm^{-1}	bending mode of Bi−I
82 cm^{-1}	asymmetric stretching of bridged Bi−I
104.5 cm^{-1}	symmetric stretch of bridging Bi−I
119.8 cm^{-1}	asymmetric stretching of terminal Bi−I
146.6 cm^{-1}	symmetric stretching of terminal Bi−I

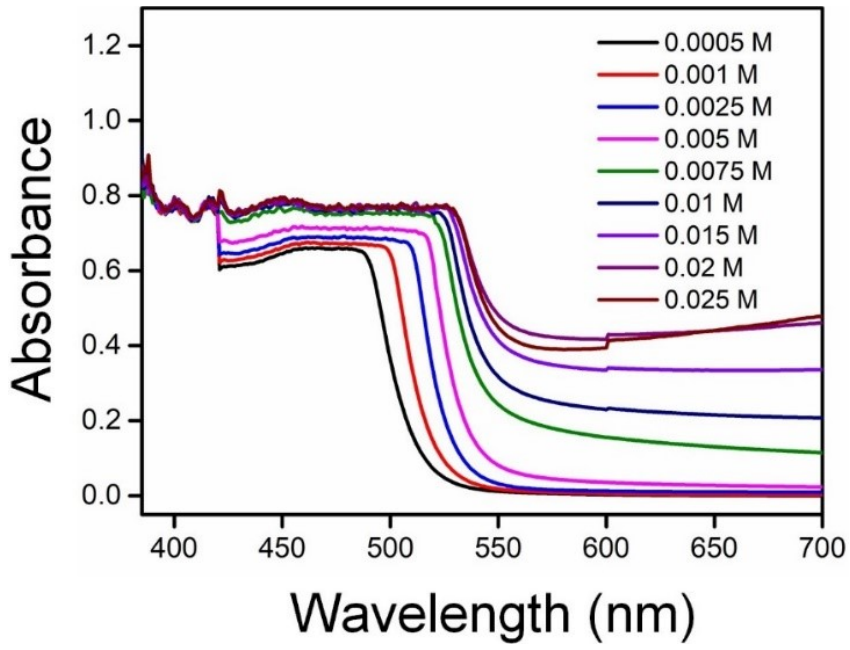

Figure S6. Absorption spectra of $Cs_3Bi_2I_9$ NDs in 6.34M aqueous HI with different molar concentrations of the NDs (in mol L^{-1}).

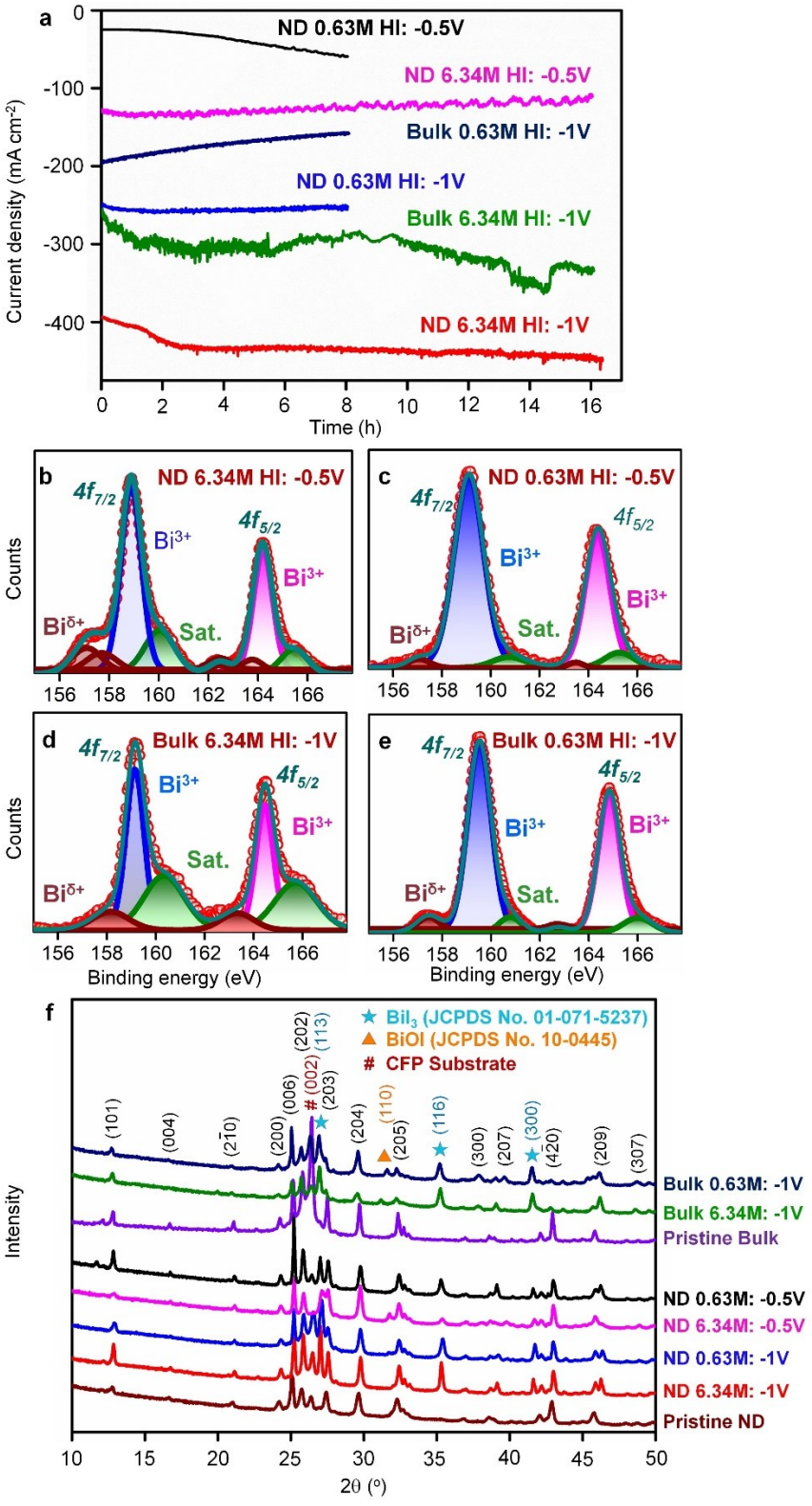

Figure S7. (a) Chronoamperometric stability plots of $Cs_3Bi_2I_9$ NDs at -0.5V and -1V versus SCE where 0.66 mg/cm^2 ND loaded CFP was dipped inside 0.005M ND saturated 0.63M and 6.34M HI solutions. Fitted XPS Bi *4f* level for the NDs in (b) 6.34M HI at -0.5V after 16h, (c) 0.63M HI at -0.5V after 8h, and for the bulk $Cs_3Bi_2I_9$ in (d) 6.34M HI at -1V after 16h, (e) 0.63M HI at -1V after 8h. The open circles are the experimental data, and the solid line represent the best fit. Sat. denotes the satellite peaks. (f) PXRD patterns of the NDs and bulk $Cs_3Bi_2I_9$ after the electrochemical stability tests.

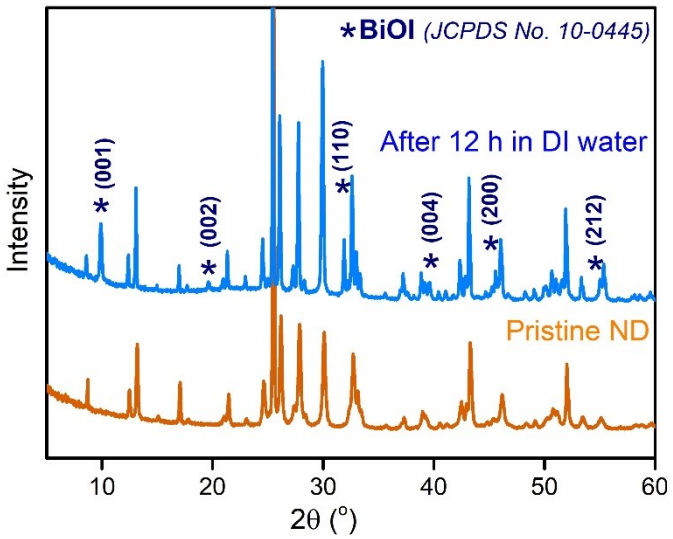

Figure S8. PXRD pattern of $Cs_3Bi_2I_9$ NDs before and after dispersing in DI water for 12h.

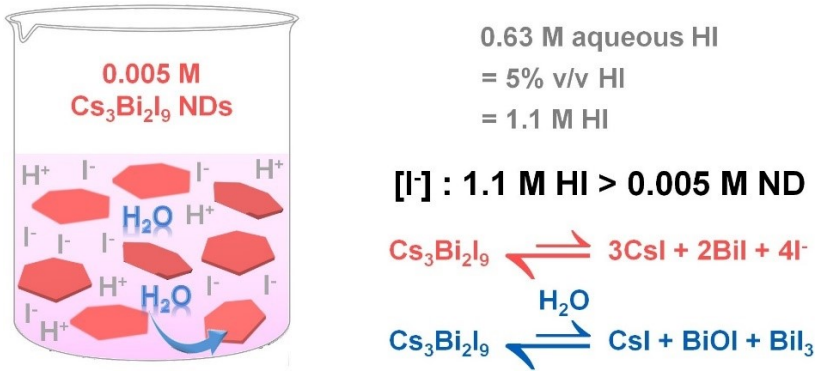

Figure S9. Schematic showing the plausible reason for the $Cs_3Bi_2I_9$ ND stability in 0.63 M saturated HI solution.

Table S1. XPS fitting parameters of $Cs_3Bi_2I_9$ ND and bulk phases after chronoamperometry tests at -0.5 and -1.0 V versus SCE, for 16h in 6.34M HI and 8h in 0.63M HI solution.

Condition	XPS levels	BE ($Bi^{\delta+}$)	Area ($Bi^{\delta+}$)	BE (Bi^{3+})	Area (Bi^{3+})	BE (Sat.)	Area (Sat.)	$Bi^{\delta+}$ Wt %	Av. $Bi^{\delta+}$ Wt%	Av. Bi^{3+} Wt%
$Cs_3Bi_2I_9$ NDs post chronoamperometry										
6.34 M -0.5 V	$4f_{7/2}$	157.1	1155.6	158.9	3211.9	160.0	1059.7	26.5	22	78
	$4f_{5/2}$	162.5	443.2	164.2	1985.4	165.5	518.8	18.2		
6.34 M -1.0 V	$4f_{7/2}$	157.0	2252.7	159.2	4518.0	160.2	819.9	33.2	28	72
	$4f_{5/2}$	162.3	957.5	164.6	3074.0	165.6	934.6	23.7		
0.63 M -0.5 V	$4f_{7/2}$	157.1	47.4	159.1	1401.9	160.8	88.7	3.3	3	97
	$4f_{5/2}$	163.5	19.7	164.4	829.3	165,3	110.9	2.3		
0.63 M -1.0 V	$4f_{7/2}$	157.6	249.4	159.1	1907.1	160.0	172.8	11.5	7	93
	$4f_{5/2}$	163.3	40.5	164.4	1449.2	165.5	146.2	2.7		

Bulk $Cs_3Bi_2I_9$ post chronoamperometry										
6.34 M -1.0 V	$4f_{7/2}$	158.1	126.8	159.1	549.0	160.3	409.8	18.8	19	81
	$4f_{5/2}$	163.3	105.6	164.4	417.6	165.7	372.7	20.2		
0.63 M -1.0 V	$4f_{7/2}$	157.5	750.5	159.5	8331.7	160.8	657.2	8.3	6	94
	$4f_{5/2}$	162.8	164.3	164.8	5706.0	166.0	830.4	2.8		

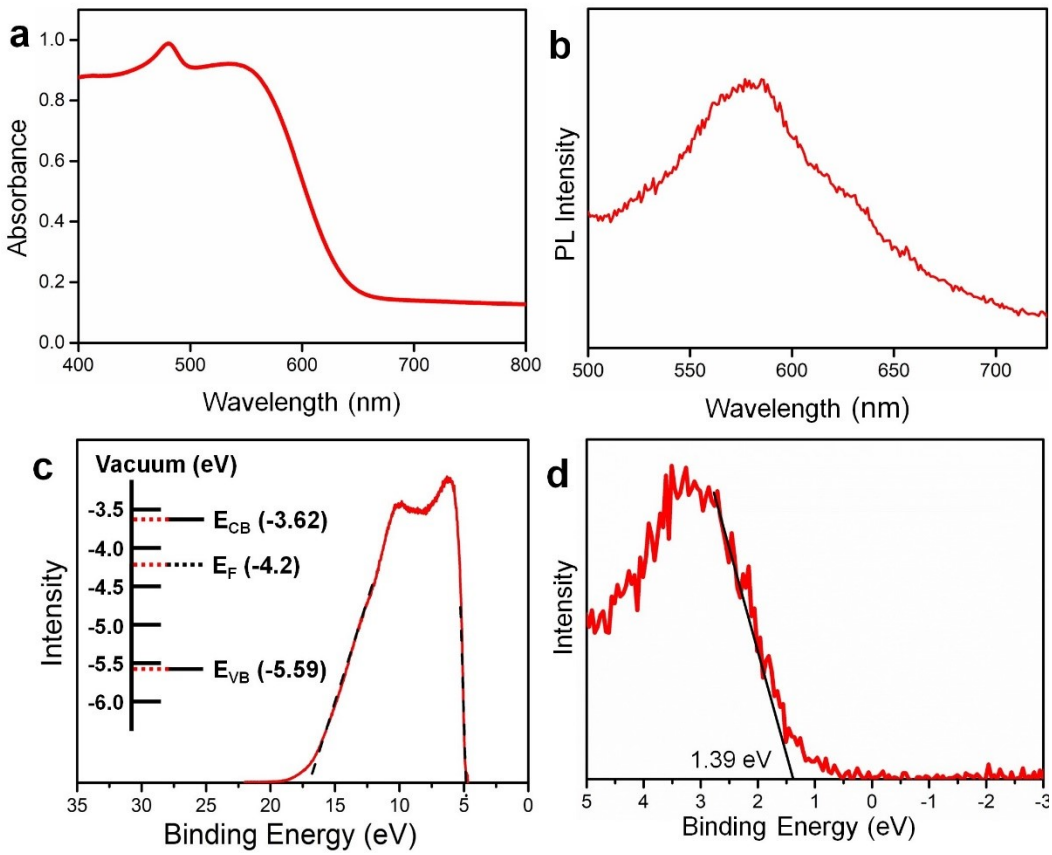

Figure S10. (a) Absorption spectrum, (b) PL spectrum, (c) UV photoelectron spectrum with inset showing the band alignment, and (d) valence band XPS spectrum of $Cs_3Bi_2I_9$ NDs.

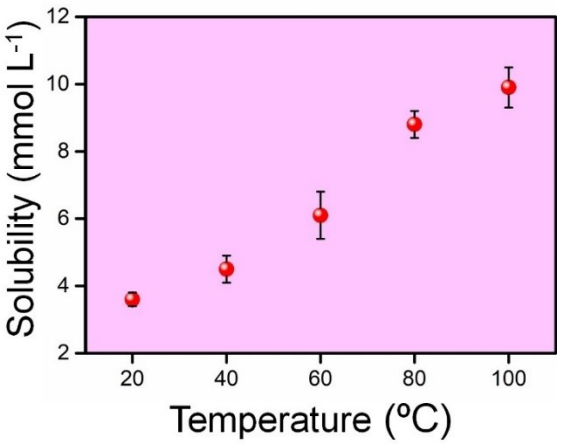

Figure S11. Solubility plot of $Cs_3Bi_2I_9$ NDs in 6.34M (50%) aqueous HI solution at different temperatures. Error bars indicate standard deviation from three trials.

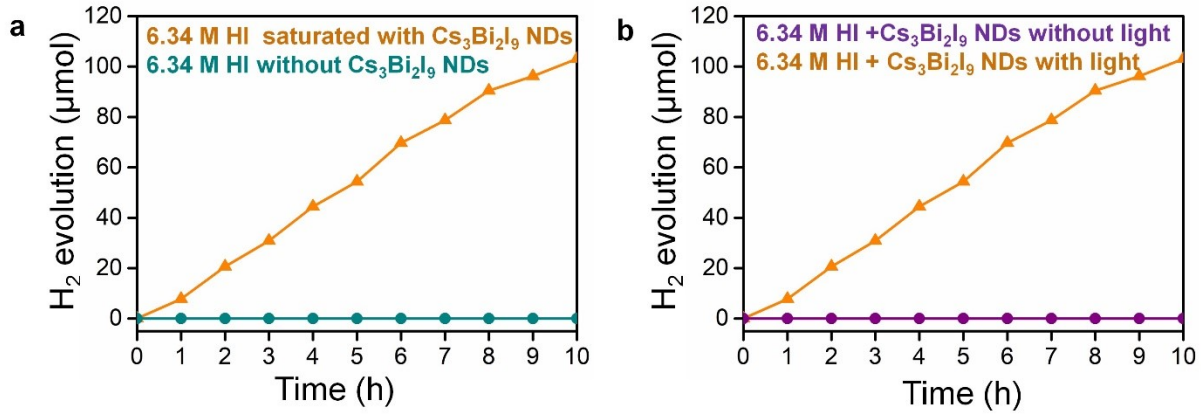

Figure S12. (a) Photocatalytic H_2 evolution by splitting of aqueous HI solution in the presence (saturation) and absence of $Cs_3Bi_2I_9$ NDs. (b) Photocatalytic H_2 evolution from 6.34M HI solution saturated by 0.005M $Cs_3Bi_2I_9$ NDs under dark condition and in the presence of visible light illumination.

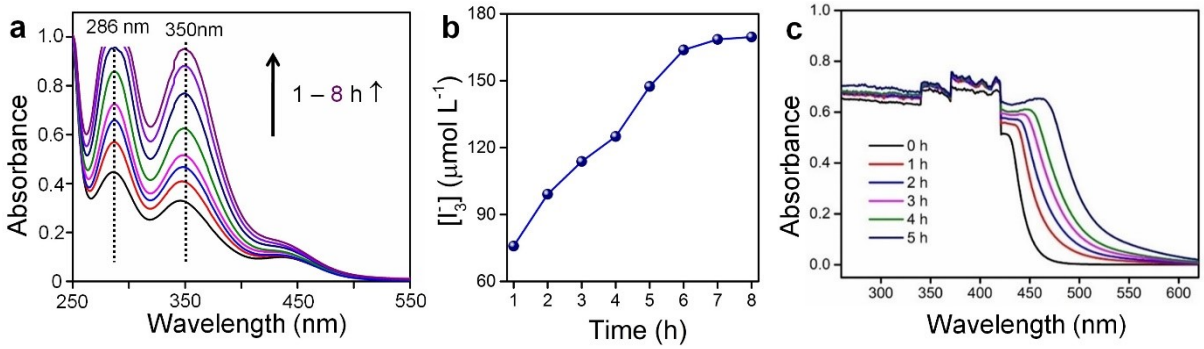

Figure S13. (a) Absorption spectra showing the temporal emergence of I_3^- ions. (b) Time dependent increase of I_3^- concentration, measured using the absorbance band at 350 nm. (c) Absorption spectra showing the absence of I_3^- ions during the photocatalytic reaction in 6.34M HBr solution saturated by 0.005M $Cs_3Bi_2I_9$ NDs.

Discussion S1. Quantum yield calculation

The quantum efficiency of HI splitting was estimated by calculating the apparent quantum efficiency (AQE) according to equation (S1):

$$AQE = \frac{Evolved\ H_2(mol) \times 6.02 \times 10^{23} \times 2 \times 0.33(eV) \times 1.6 \times 10^{-19}}{P_{sol}(Wcm^{-2}) \times Area(cm^2) \times time(s)} \times \quad \text{(S1)}$$

The evolved gas by photocatalytic HI splitting = 11.3 µmol h^{-1};

Avogadro Number = 6.022×10^{23};
P_{sol} is the power density of the incident monochromatic light = 450 W lamp calibrated to 150 $mWcm^{-2}$; Area = Irradiated area to produce (mol) of hydrogen = 0.2 cm^2;
Irradiated time = 1 h = 3600 s; Electronic charge = 1.6×10^{-19} C
Since H^+/H_2 reduction potential is 0.046V versus NHE and I^-/I_3^- oxidation potential is 0.376V versus NHE, the total potential for HI splitting is 0.376 V − 0.046 V = 0.33 V.

Hence, AQE is calculated as 0.66 % ~ 0.7%. With H_3PO_2 and Pt co-catalyst, 22.5μmol h^{-1} H_2 is equivalent to a quantum efficiency of 1.3%.

Table S2. Comparative list of the photocatalytic HI splitting activity by pristine and composite metal-halide perovskites with respect to $Cs_3Bi_2I_9$ NDs.

Photocatalysts	**Light source (λ in nm)**	**Reaction medium**	**H_2 activity**	**Ref.**
$Cs_3Bi_2I_9$ NDs	150 mW cm^{-2} Xe lamp (λ ≥ 420 nm)	Saturated HI	11.3 μmol h^{-1}	This work
$Cs_3Bi_2I_9$ NDs /Pt	150 mW cm^{-2} Xe lamp (λ ≥ 420 nm)	Saturated HI	22.5 μmol h^{-1}	This work
$MAPbI_3$	300 W Xe lamp (λ > 475 nm)	Saturated HI	30.0 μmol $h^{-1}g^{-1}$	S1
$MAPbI_3$/Pt	100 W solar simulator (λ > 475 nm)	Saturated HI	57 μmol $h^{-1}g^{-1}$	S1
$MAPbBr_{3-x}I_x$/Pt	300 W Xe lamp (λ ≥ 420 nm)	Saturated HI/HBr	651.2 μmol h^{-1}	S2
$CsPbBr_{3-x}I_x$/Pt	300 W Xe lamp (λ ≥ 420 nm)	Saturated HI/HBr	224 μmol h^{-1}	S3
$MAPbI_3$/Pt/TiO_2	300 W Xe lamp (λ > 420 nm)	Saturated HI	29 μmol h^{-1}	S4
$MAPbI_3$/rGO	300 W Xe lamp (λ ≥ 420 nm)	Saturated HI	93.9 μmol h^{-1}	S5
$MAPb(I_{0.9}Br_{0.1})_3$	300 W Xe lamp (λ ≥ 420 nm)	Saturated HI/HBr	1471 μmol $h^{-1}g^{-1}$	S6
$Ni_3C/MAPbI_3$	300 W Xe lamp (λ ≥ 420 nm)	Saturated HI	2362 μmol $h^{-1}g^{-1}$	S7
$MA_3Bi_2I_9$/Pt	300 W (λ ≥ 400 nm)	Saturated HI	169 μmol h^{-1}	S8
$MAPbI_3$/ (piezoelectric)	100 mW cm-2 (λ ≥ 420 nm)	Saturated HI	23.30 μmol h^{-1}	S9
$[(CH_3)_2NH_2]_3[BiI_6]$ (PtI_x)	465 nm LED	Saturated HI	---	S10
$MA_3Bi_2I_9$/ DMA_3BiI_6	300 W Xe lamp (λ ≥ 420 nm)	Saturated HI	198.2 μmol $h^{-1}g^{-1}$	S11
$MAPbI_3$/cobalt phosphide	150 W Xe lamp (λ ≥ 420 nm)	Saturated HI	785.9 μmol $h^{-1}g^{-1}$	S12
$Cs_3Bi_{0.6}Sb_{1.4}I_9$	100 W solar simulator	Saturated HI	92.6 μmol h^{-1}	S13

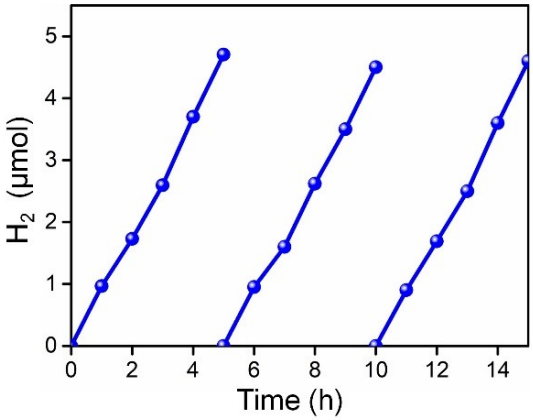

Figure S14. Recyclability test of the NDs for three 5h runs in 0.63M aqueous HI.

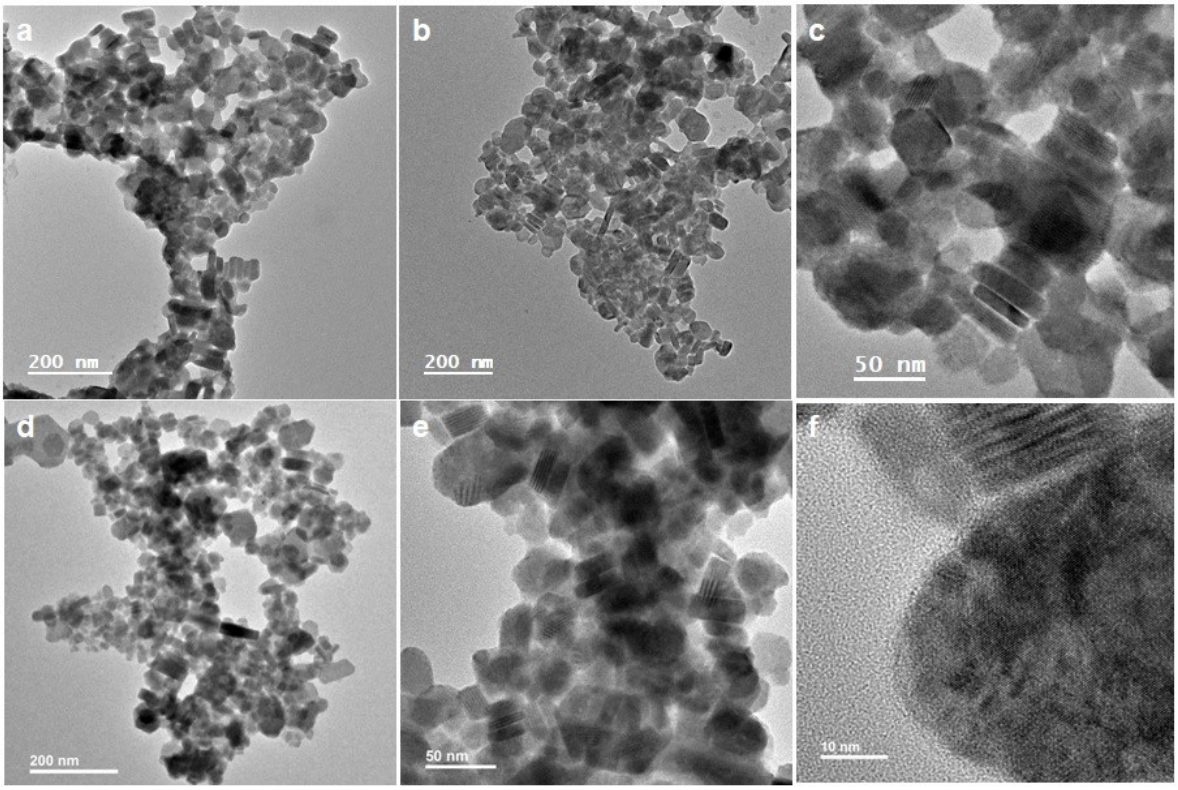

Figure S15. Additional TEM images of $Cs_3Bi_2I_9$ NDs after 10h photocatalysis in 0.005 M ND saturated (a-c) 6.34 M and (d-f) 0.63 M aqueous HI solutions.

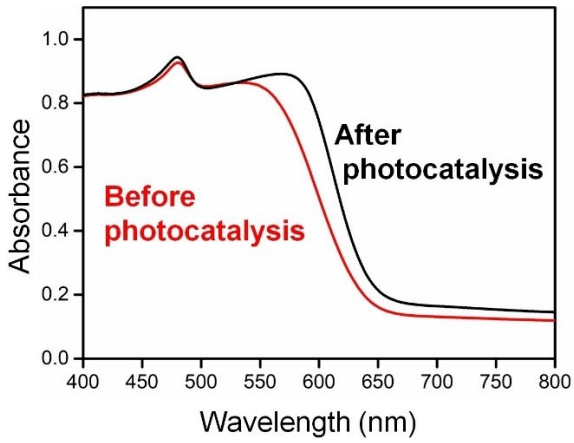

Figure S16. Absorption spectra of $Cs_3Bi_2I_9$ NDs before and after 10h photocatalysis.

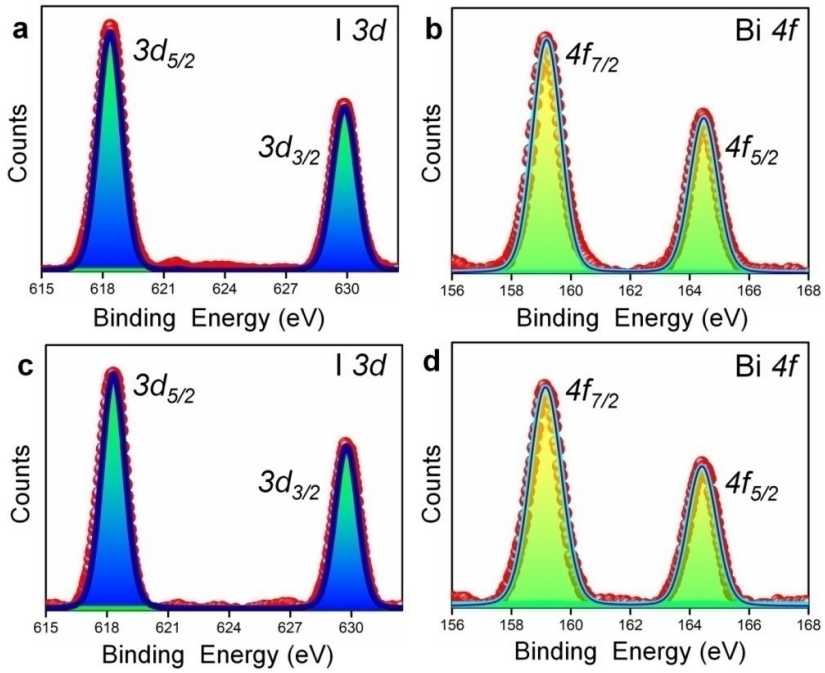

Figure S17. XPS spectra of $Cs_3Bi_2I_9$ NDs (a, b) before and (c, d) after photocatalysis. The C *1s* binding energy of 284.8 eV was used as reference.

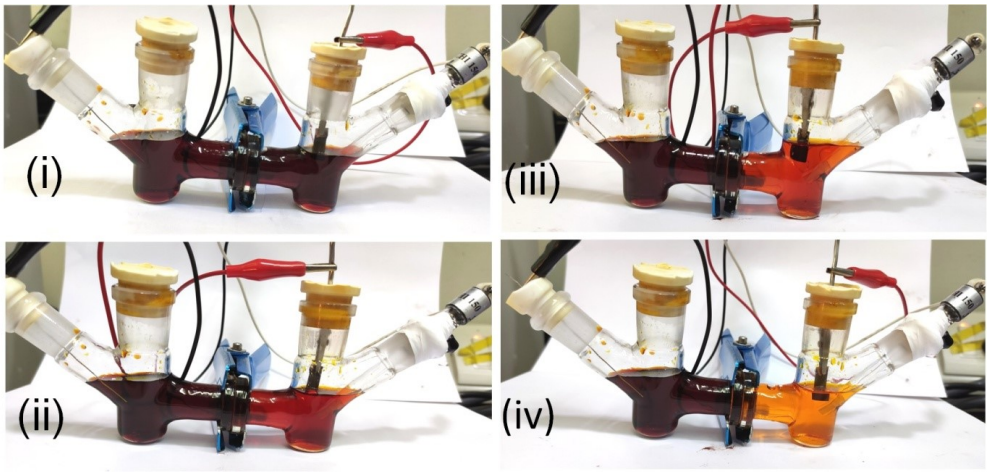

Figure S18. (a) Digital images of the H-cell containing ND saturated aqueous HI solution (i) before, and after electrochemical reduction for (ii) 1h, (iii) 2h, and (iv) 3h. A proton exchange membrane (Nafion) between left and the right slots of the H-cell, allows the solution color to change exclusively in the right slot from dark brown to light yellowish orange due to the continuous electrochemical reduction of I_3^- to I^- over time.

Discussion S2: TOF calculation

The number of hydrogen turnover is calculated from the current density according to:

$$\text{Number of hydrogen turnover} = \left(j\frac{mA}{cm^2}\right)\left(\frac{1\ C/s}{1000\ mA}\right)\left(\frac{1\ mol\ e-}{96485.3\ C}\right)\left(\frac{1\ mol\ H_2}{2\ mol\ e-}\right) \times (6.023 \times 10^{23})$$

<u>For 6.34M HI Saturated $Cs_3Bi_2I_9$ NDs</u>

Specific capacitance (C_s) = 0.04 mF/cm^2
Double layer capacitance (C_{dl}) = 2.4 mF

$$\text{ECSA} = \frac{Cdl}{Cs} = \frac{2.4}{0.04} = 60\ \text{cm}^2$$

At 533 mV overpotential, $Cs_3Bi_2I_9$ NDs reach a current density of -100 mAcm^{-2}.

Number of hydrogen turnover for $Cs_3Bi_2I_9$ NDs at 533 mV overpotential:

$$\left(100\frac{mA}{cm^2}\right)\left(\frac{1\ C/s}{1000\ mA}\right)\left(\frac{1\ mol\ e-}{96485.3\ C}\right)\left(\frac{1\ mol\ H_2}{2\ mol\ e-}\right) \times (6.023 \times 10^{23}) = 3.1212 \times 10^{17}\left(\frac{1/s}{cm^2}\right)$$

Based on ECSA along with the unit cell volume (1295.66 Å^3) of $Cs_3Bi_2I_9$ NDs, active sites per real surface area:

$$\text{Active Surface sites} = \left(\frac{2\ atom/unit\ cell}{1293.96\ Å^3/unit\ cell}\right)^{2/3} = 0.0133\times10^{16} atoms\ cm^{-2}_{real}$$

$$\text{TOF } (\eta_{533}) = \frac{3.122\ x\ 10^{17}\left(\frac{1/s}{cm^2}\right)\ \times\ 0.3\ cm^2}{Active\ Surface\ sites\ \times\ ECSA} = 11.736\ s^{-1}$$

Therefore, TOF of $Cs_3Bi_2I_9$ NDs for HER is 11.7 s^{-1} at an overpotential of 533 mV.

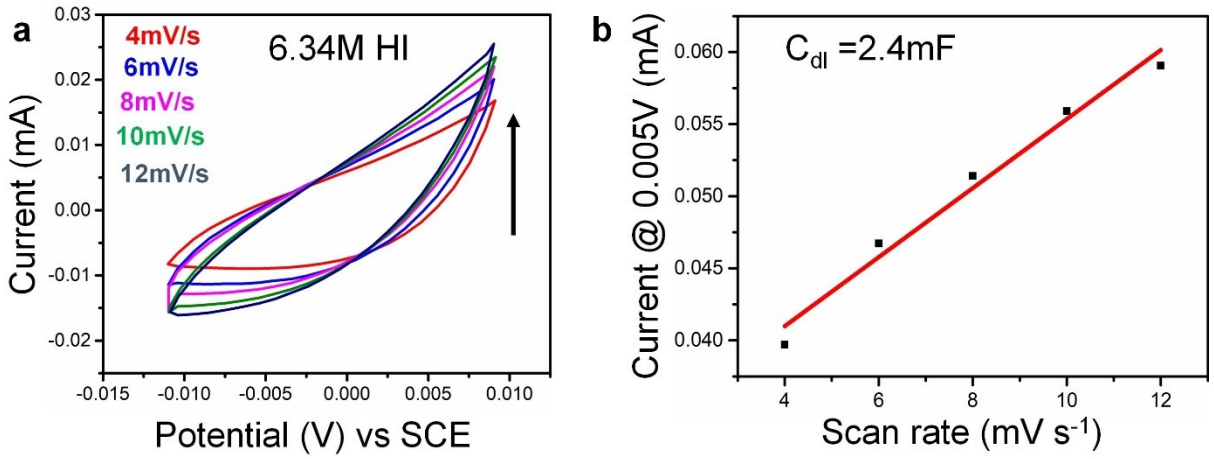

Figure S19. ECSA determination of $Cs_3Bi_2I_9$ ND electrocatalyst. (a) CV cycles at different scan rates. (b) Current density as function of scan rate at fixed overpotential.

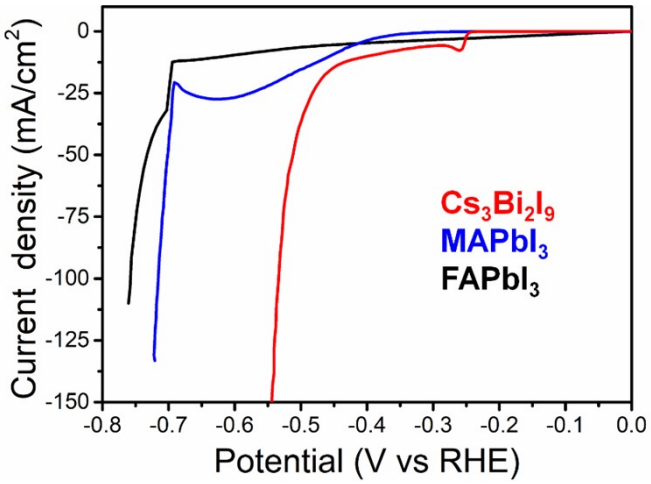

Figure S20. LSV polarization curves showing the electrochemical HER activity of $Cs_3Bi_2I_9$ NDs, $MAPbI_3$ and $FAPbI_3$ [MA: CH_3NH_3, FA: $HC(NH_2)_2$].

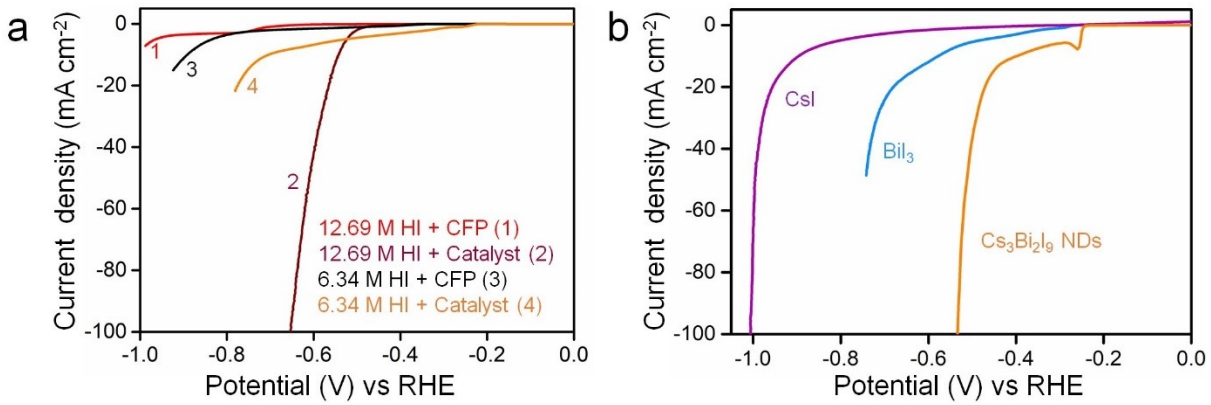

Figure S21. (a) LSV polarization plots in different electrolyte and catalyst combinations. (b) Comparison of electrochemical HI splitting activity of $Cs_3Bi_2I_9$ NDs with CsI and BiI_3.

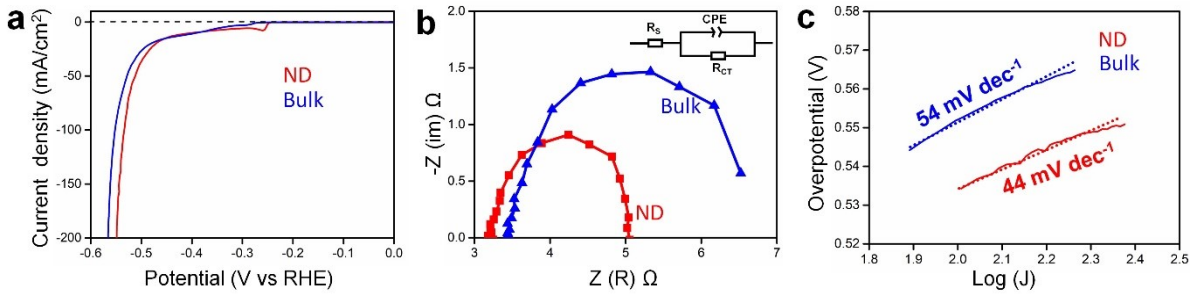

Figure S22. Comparison of the electrocatalytic HER activity between the NDs and bulk $Cs_3Bi_2I_9$ in 6.34M HI. (a) LSV polarization plots, (b) Nyquist plots measured at 700 mV overpotential (*iR* uncorrected), and (c) Tafel plots with the corresponding Tafel slopes.

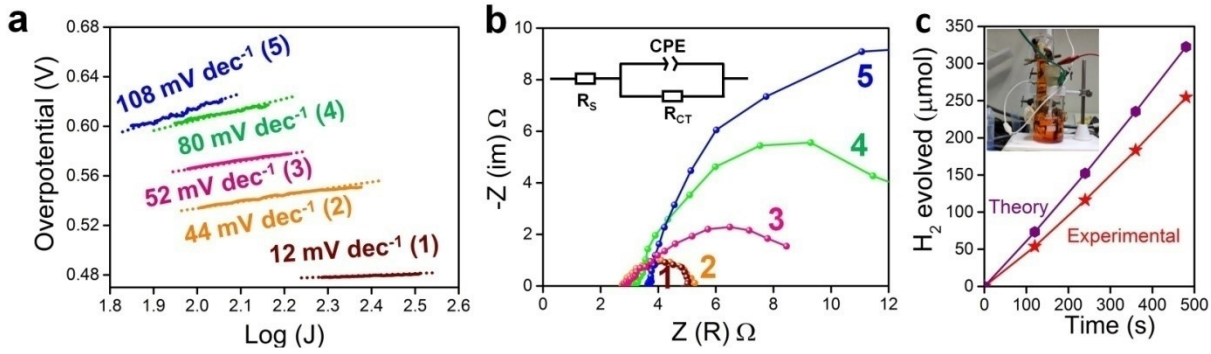

Figure S23. (a) Tafel plots and their corresponding Tafel slopes. (b) Nyquist plots measured at 700 mV overpotential (*iR* uncorrected) for HER. Inset shows the equivalent circuit (R_S: solution resistance; CPE: constant phase element; R_{CT}: charge transfer resistance). (c) Faradaic efficiency measured at 1V overpotential (*iR* uncorrected) showing the theoretically calculated and experimentally measured H_2 gas with time. Inset shows digital image of the measurement setup. The samples: (1) 12.69 M HI, (2) 6.34 M HI, (3) 3.17 M HI, (4) 1.26 M HI, and (5) 0.63 M HI.

Supporting References

S1 S. Park, W. Chang, C. Lee, S. Park, H. Ahn, K. Nam, *Nat. Energy*, 2017, **2**, 16185.

S2 Y. Wu, P. Wang, Z. Guan, J. Liu, Z. Wang, Z. Zheng, S. Jin, Y. Dai, M. Whangbo, B. Huang, *ACS Catal.*, 2018, **8**, 10349-10357.

S3 Z. Guan, Y. Wu, P. Wang, Q. Zhang, Z. Wang, Z. Zheng, Y. Liu, Y. Dai, M. Whangbo, B. Huang, *Appl. Catal. B: Environ.*, 2019, **245,** 522-527.

S4 X. Wang, H. Wang, H. Zhang, W. Yu, X. Wang, Y. Zhao, X. Zong, C. Li, *ACS Energy Lett.*, 2018, **3**, 1159-1164.

S5 Y. Wu, P. Wang, X. Zhu, Q. Zhang, Z. Wang, Y. Liu, G. Zou, Y. Dai, M. Whangbo, B. Huang, *Adv. Mater.*, 2018, **30**, 1704342.

S6 Z. Zhao, J. Wu, Y. Zheng, N. Li, X. Li, Z. Ye, S. Lu, X. Tao, C. Chen, *Appl. Catal. B: Environ.*, 2019, **253**, 41-48.

S7 Z. Zhao, J. Wu, Y. Zheng, N. Li, X. Li, X. Tao, *ACS Catal.*, 2019, **9**, 8144-8152.

S8 Y. Guo, G. Liu, Z. Li, Y. Lou, J. Chen, Y. Zhao, *ACS Sustain. Chem. Eng.*, 2019, **7**, 15080-15085.

S9 M. Wang, Y. Zuo, J. Wang, Y. Wang, X. Shen, B. Qiu, L. Cai, F. Zhou, S. Lau, Y. Chai, *Adv. Energy Mater.*, 2019, **9**, 1901801.

S10 H. Zhao, Y. Li, B. Zhang, T. Xu, C. Wang, *Nano Energy*, 2018, **50**, 665-674.

S11 Y. Tang, C. Mak, R. Liu, Z. Wang, L. Ji, H. Song, C. Tan, F. Barrière, H. Hsu, *Adv. Funct. Mater.*, 2020, **30**, 2006919.

S12 C. Cai, Y. Teng, J. Wu, J. Li, H. Chen, J. Chen, D. Kuang, *Adv. Funct. Mater.*, 2020, **30**, 2001478.

S13 G. Chen, P. Wang, Y. Wu, Q. Zhang, Q. Wu, Z. Wang, Z. Zheng, Y. Liu, Y. Dai, B. Huang, *Adv. Mater.*, 2020, **32**, 2001344.